

the allowable achromatic bandwidth is 0.97% or $(\lambda/\Delta\lambda) = 103$, we see that a thickness difference of up to 1.5 mm between the refractive lens and the refractive Fresnel lens profile still satisfies the coherence length requirement for the bandwidth used. It is this net thickness difference that is the important parameter; one could go up to this limit in $(\lambda/\Delta\lambda) = 103$ steps of 2π phase change, or 34 steps of 6π phase change, to pick two examples. Finally, since the radius r of a plano-convex lens with a thickness t at its centre is given by $r = \sqrt{2R_C t - t^2}$, with $R_C = 5.6$ mm and $t = 1.5$ mm one can have a lens radius up to 3.8 mm (or a numerical aperture of up to 0.75) and still remain within the coherence length requirement of a Fresnel lens with 0.93% bandwidth.

In practice, one can imagine lithographically fabricating an achromatic Fresnel optic (AFO) on a single thin membrane, with the Fresnel zone plate fabricated on one side, and a refractive Fresnel lens on the other side, as shown in Fig. 1 (possibly fabricated using multilevel^{21,22} or imprint²³ methods). The achievable efficiencies of the zone plate and the Fresnel lens are about 30–50% and 30–80%, respectively, leading to a combined efficiency of 10–40% for the AFO which compares quite favourably with, for example, the ~5% net throughput of a next-generation lithography system using six optics with 60% reflectivity each to gain the required resolution and field of view.

The size of the AFO and its imaging field are likely to be limited by primary aberrations. Seidel wavefront aberrations for imaging finite conjugates with zone plate optics have been calculated by Young²⁴. At 1.34-nm wavelength (Cu L absorption edge) with a 4:1 demagnifying geometry (a standard set-up used in lithography cameras), aberration-free imaging fields of between 2 and 15 mm can be expected for outermost zone widths between 40 and 95 nm without aberration correction. When used with EUV radiation near 12.5 nm wavelength, the NAs are increased nearly tenfold and primary aberrations become more problematic unless the field of view is kept to a few tenths of 1 mm. Spherical aberration does not exist for Fresnel zone plates when the zone placement is computed for a specific imaging geometry. This property, along with the achromatic nature of the AFO, allows one to reduce the field curvature and astigmatism to an acceptable level by increasing the AFO diameter (therefore the focal length) while maintaining the same field of view. Coma can be reduced and eliminated in some cases by appropriate aperturing.

In general, the AFO design provides two important benefits: it makes a large bandwidth of electromagnetic radiation usable, and it allows large-diameter high-resolution optics to be produced without suffering from chromatic aberration. The increased bandwidth should greatly improve the throughput of applications using broadband X-ray sources, such as X-ray tubes and laser-produced plasmas. In addition, non-spectroscopic imaging applications such as tomography at synchrotron radiation sources could operate with reduced imaging time using multilayer monochromators rather than narrow-bandpass crystal monochromators. The large diameter gives large working distance and large imaging field, both valuable attributes in imaging applications. The present AFO design has the potential to make significant impact in X-ray microscopy and microanalysis, and next-generation lithography applications. □

Received 27 January; accepted 19 May 2003; doi:10.1038/nature01756.

1. Meyer-Ilse, W., Warwick, T. & Attwood, D. (eds) *X-ray Microscopy: Proceedings of the Sixth International Conference* (American Institute of Physics, Melville, New York, 2000).
2. Chapman, H. N. *et al.* First lithographic results from the extreme ultraviolet engineering test stand. *J. Vac. Sci. Technol. B* **19**, 2389–2395 (2001).
3. Peuker, M. High-efficiency nickel phase zone plates with 20 nm minimum outermost zone width. *Appl. Phys. Lett.* **78**, 2208–2210 (2001).
4. Röntgen, W. C. Über eine neue Art von Strahlen. Vorläufige Mittheilung. *Sber. Phys.-Med. Ges. Würzb.* **137**, 132–141 (1895).
5. Röntgen, W. C. On a new kind of rays. *Nature* **53**, 274–276 (1896).
6. Einstein, A. Lassen sich Brechungsexponenten der Körper für Röntgenstrahlen experimentell ermitteln? *Verh. Dtsch. Phys. Ges.* **20**, 86–87 (1918).

7. Kirkpatrick, P. & Baez, A. V. Formation of optical images by x-rays. *J. Opt. Soc. Am.* **38**, 766–774 (1948).
8. Hignette, O. *et al.* in *X-ray Micro- and Nano-Focusing: Applications and Techniques II* (ed. McNulty, I.) 105–116 (Proc. SPIE, The International Society for Optical Engineering, San Diego, 2001).
9. Baez, A. V. A self-supporting metal Fresnel zone-plate to focus extreme ultra-violet and soft X-rays. *Nature* **186**, 958 (1960).
10. Michette, A. G. *Optical Systems for Soft X-Rays* (Plenum, New York, 1986).
11. Yang, B. X. Fresnel and refractive lenses for X-rays. *Nucl. Instrum. Meth. Phys. Res. A* **328**, 578–587 (1993).
12. Snigirev, A., Kohn, V., Snigireva, I. & Lengeler, B. A compound refractive lens for focusing high energy X-rays. *Nature* **384**, 49–51 (1996).
13. Lengeler, B. *et al.* Parabolic refractive X-ray lenses. *J. Synchrotron Radiat.* **9**, 119–124 (2002).
14. Spiller, E. Low-loss reflection coatings using absorbing materials. *Appl. Phys. Lett.* **20**, 365–367 (1972).
15. Naulleau, P. *et al.* Sub-70-nm EUV lithography at the Advanced Light Source static microfield exposure station using the ETS Set-2 optic. *J. Vac. Sci. Technol. B* **20**, 2829–2833 (2002).
16. Henke, B. L., Gullikson, E. M. & Davis, J. C. X-ray interactions: photoabsorption, scattering, transmission, and reflection at $E = 50$ –30,000 eV, $Z = 1$ –92. *At. Data Nucl. Data Tables* **54**, 181–342 (1993).
17. Dobson, S. L., Sun, P.-C. & Fainman, Y. Diffractive lenses for chromatic confocal imaging. *Appl. Opt.* **36**, 4744–4748 (1997).
18. Michette, A. G., Buckley, C., Gallo, E., Powell, K. & Pfauntsch, S. J. in *Advances in X-ray Optics* (ed. Freund, A. K. *et al.*) 303–310 (Proceedings SPIE Vol. 4145, The International Society for Optical Engineering, Bellingham, Washington, 2000).
19. Hendrickson, W. A. Determination of macromolecular structures from anomalous diffraction of synchrotron radiation. *Science* **254**, 51–58 (1991).
20. Jackson, J. D. *Classical Electrodynamics* (Wiley & Sons, New York, 1975).
21. Stern, M. B. & Medeiros, S. S. Deep three-dimensional microstructure fabrication for infrared binary optics. *J. Vac. Sci. Technol. B* **10**, 2520–2525 (1992).
22. Walsby, E. D. *et al.* Multilevel silicon diffractive optics for terahertz waves. *J. Vac. Sci. Technol. B* **20**, 2780–2783 (2002).
23. Hirai, Y. *et al.* Imprint lithography for curved cross-sectional structure using replicated Ni mold. *J. Vac. Sci. Technol. B* **20**, 2867–2871 (2002).
24. Young, M. Zone plates and their aberrations. *J. Opt. Soc. Am.* **62**, 972–976 (1972).
25. van Buuren, T. W. H. *et al.* Electronic structure of silicon nanocrystals as a function of particle size. *Abstr. Pap. Am. Chem. Soc.* **213**, 313 (1997).
26. Liu, R. S. *et al.* Evidence for electron-doped (*n*-type) superconductivity in the infinite-layer $(\text{Sr}_{0.9}\text{La}_{0.1})\text{CuO}_2$ compound by X-ray absorption near-edge spectroscopy. *Solid State Commun.* **118**, 367–370 (2001).
27. Dambach, S. *et al.* Novel interferometer in the soft x-ray region. *Phys. Rev. Lett.* **80**, 5473–5476 (1998).

Acknowledgements We thank J. Kirz for discussions, and S. Frigo for information about the calculation of Kramers–Kronig transforms.

Competing interests statement The authors declare competing financial interests: see the website (<http://www.nature.com>) for details.

Correspondence and requests for materials should be addressed to W.Y. (wyun@xradia.com).

Asymmetric pores in a silicon membrane acting as massively parallel brownian ratchets

Sven Matthias & Frank Müller

Max Planck Institute of Microstructure Physics, Weinberg 2, Halle 06120, Germany

The brownian motion of mesoscopic particles is ubiquitous and usually random. But in systems with periodic asymmetric barriers to movement, directed or ‘rectified’ motion can arise and may even modulate some biological processes¹. In man-made devices, brownian ratchets and variants based on optical or quantum effects have been exploited to induce directed motion^{2–14}, and the dependence of the amplitude of motion on particle size has led to the size-dependent separation of biomolecules^{6,8,15}. Here we demonstrate that the one-dimensional pores of a macroporous silicon membrane¹⁶, etched to exhibit a periodic asymmetric variation in pore diameter, can act as massively parallel and multiply stacked brownian ratchets that are potentially suitable for large-scale particle separations. We

show that applying a periodic pressure profile with a mean value of zero to a basin separated by such a membrane induces a periodic flow of water and suspended particles through the pores, resulting in a net motion of the particles from one side of the membrane to the other without moving the liquid itself. We find that the experimentally observed pressure dependence of the particle transport, including an inversion of the transport direction, agrees with calculations^{17,18} of the transport properties in the type of ratchet devices used here.

Particle separation is often accomplished by exploiting the dependence of drift or diffusion on size. That is, the process starts with a mixture, and as the particles move with different velocities, different components can be picked up at different positions away from the starting point. In contrast, ratchet-based devices¹⁴ tend to exploit changes in drift direction as a function of particle size, which can in principle lead to smaller devices capable of continuous operation. Microscopic calculations of the transport of particles in ratchet devices similar to those used here have revealed the closely related effects of the dependence of the net motion direction of the particles on particle size (for a fixed pressure) and on pressure amplitude (for fixed particle size)¹⁷. In these experiments, we demonstrate that the transport in our membranes exhibits the predicted pressure dependence.

Our experimental set-up consists of two basins filled with an aqueous solution of dispersed particles and separated by a horizontally mounted ratchet membrane (Fig. 1). The upper basin is open, and the lower basin closed and connected to an electrically driven pressure oscillator. The pore arrays were grown by a photo-electrochemical etching process^{19,20}, which has been extended to allow very strong diameter modulations^{16,21,22}. The particles were commercial luminescent polystyrene spheres with well-defined diameters of 0.1 μm , 0.32 μm , 0.53 μm and 1 μm , respectively. The concentration used was approximately one particle per pore. Interactions between the beads can therefore be neglected. The total number of particles in the upper basin was measured by photoluminescence (PL).

Applying square wave pressure oscillations to the lower basin generated a periodic back and forth streaming of the water-plus-particle system between the two basins through the membrane. By simultaneously recording the pressure in the lower basin and the filling level in the upper basin, we could investigate the water flow.

For carefully prepared hydrophilic pore walls and hyper-pure water as carrier liquid, the well-known macroscopic hydrodynamic equations are appropriate. The flow through the straight pores can be described by the Hagen–Poiseuille law. For the shaped pores the flow was still well approximated by the Hagen–Poiseuille law when using the minimum diameter. In addition, the oscillations of the particles together with the carrying water through the capillaries was directly observed by lock-in PL-spectroscopy using the pressure oscillations as reference signal. We modulated our whole experiment and toggled the driving pressure oscillations on and off every 60 seconds to exclude long-term drifts caused, for example, by water evaporation. This toggling also enables us to obtain more information about the system. Together with the macroscopic simulations presented later, this helps us to understand in more detail the drift and diffusion contributions.

In Fig. 2a the curve labelled U shows the evolution of the PL signal, starting from a homogeneous particle distribution. The applied root-mean-square (r.m.s.) pressure during the ‘on’ phase is 2,000 Pa with a frequency of 40 Hz. The ‘on’ phases of the cycles are highlighted in grey. When switched on for the first time at $t = 60$ s, the PL signal increases nearly linearly with time. After 60 s the total PL intensity and therefore the total number of particles in the upper basin has increased by about 8%. Turning off the periodic pressure oscillations leads to a nearly constant signal. Only a very slight decrease is visible. Repeating this cycle several times, we observe an increase of the signal during the ‘on’ phases of the cycles, although for longer times the number of added particles is reduced. On the other hand, during the ‘off’ phases the number of vanishing particles strongly increases with time. The profile changes from a stepwise function to a sawtooth-like behaviour and suggests the onset of a mechanism that pushes the particles back into the membrane.

Our experimental set-up does not permit us to measure the PL in the lower basin. In a second experiment we therefore mounted the membrane with reversed orientation. In Fig. 2a the curve labelled U_{reversed} shows the corresponding PL evolution. There is no pronounced systematic correlation with the ‘on’ and ‘off’ phases to be seen, but the number of particles is, except for some perturbations, clearly decreasing with time. A second control experiment was performed using straight cylindrical pores with a diameter of 2.4 μm . Curve $U_{\text{cylindrical}}$ in Fig. 2a shows that particle transport is

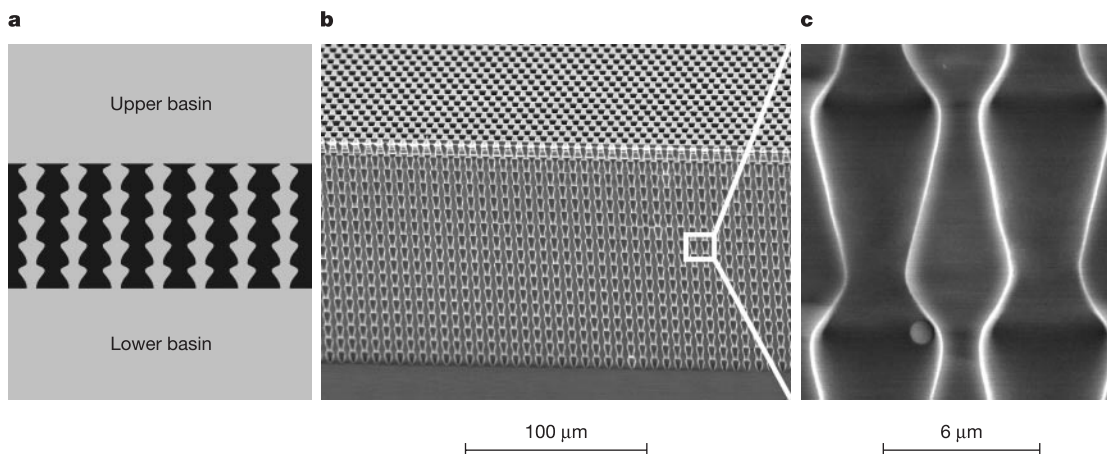


Figure 1 Experimental set-up. **a**, Schematic representation. The horizontally mounted membrane structure with asymmetric diameter modulated pores separates two basins, upper and lower. **b**, Scanning electron micrograph of a cleaved modulated macroporous silicon wafer. The macropores are arranged in a triangular lattice with a pitch of 6 μm and

a depth of about 150 μm . **c**, Scanning electron micrograph of a cleaved modulated macroporous silicon ratchet membrane. After drying, some colloidal spheres with a diameter of 1 μm stick to the silicon surface. The maximum pore diameter is 4.8 μm and the minimum 2.5 μm . The length of one period is 8.4 μm .

indeed only observable for the shaped pores.

Two processes are superimposed during the water-plus-particle oscillations: the brownian motion of the particles and its oscillations through the channel itself. The particle is diffusing randomly between liquid layers of different speed. Owing to the spatial asymmetry the liquid velocity field, and hence the friction forces onto the beads, possess a ratchet-like profile, enabling uni-directional motion^{12,17}. At present there are no convincing 'hand-waving' arguments for why the direction of transport depends on the amplitude of the applied pressure, as predicted by the numerical calculations.

The transport was microscopically modelled¹⁷ by solving the equation of motion for a single particle in an infinitely long pore given by the Langevin equation:

$$\dot{\mathbf{x}}(t) = \mathbf{v}(\mathbf{x}(t), t) + \sqrt{2D_0}\xi(t) \quad (1)$$

Here D_0 is the diffusion coefficient, $\xi(t)$ the independent gaussian noise and $\mathbf{v}(\mathbf{x}(t), t)$ the velocity field of the liquid. The microscopic calculations result in a systematic particle drift with a drift velocity v_m in the range of $\pm 1 \mu\text{m s}^{-1}$, depending on particle size and pressure amplitude. In addition, the calculations show that under these conditions the spreading of a particle ensemble can be described by an enhanced diffusion coefficient of the particles

$D_{\text{eff}} = rD_0$. Typically the enhancement factor r is in the range 1 to 10.

To understand the experimental data of Fig. 2a, we modelled the macroscopic system by a one-dimensional diffusion equation for the particle density $n(z, t)$.

$$\frac{\partial n}{\partial t} = -\frac{\partial}{\partial z}(j_{\text{drift}} + j_{\text{diffusion}}) = -\frac{\partial}{\partial z}\left(nv_m - \frac{\partial}{\partial z}(Dn)\right) \quad (2)$$

Typical parameters were taken from microscopic theory¹⁷. A transition region of $20 \mu\text{m}$ was introduced between membrane and basin where the parameters evolve gradually to reflect the smoothing caused by the oscillations.

The total number of particles in the upper and lower basins is shown in Fig. 2b. Comparing the results of the simulation for the upper basin with the experimental behaviour in Fig. 2a (U) we observe excellent qualitative agreement. All the characteristic peculiarities are reproduced. The signals show the same behaviour going from a stepwise function to a more sawtooth-like profile. After about 700 s some sort of saturation is observed where the net increase of particles over one cycle is strongly reduced compared to the beginning of the experiment. The evolution for the lower basin in the simulation again qualitatively reproduces the smooth, unstructured signal of the experiment with reversed mounted membrane (U_{reversed}).

Looking at the position dependence of the concentration profile (Fig. 3), we can immediately understand the reason for the observed evolutions. During the 'on' phases of the cycles the particles drift from the membrane to the upper basin. Since outside the membrane there is no drift, the particles accumulate near the surface. A large gradient towards the membrane evolves over time. This leads to the strong back-diffusion that is visible as soon as the drift is shut off. After 720 s almost the whole membrane is depleted. The net transport capacity of the membrane is limited by the few particles that diffuse into the membrane from the lower basins. The particles from the upper basin mostly diffuse back into the surface region of the membrane during the 'off' phase, only to be driven out again during the 'on' phase. Thus the characteristic triangular profile evolves. The low diffusion current into the volume of the upper basin and the limited diffusion current of particles from the lower

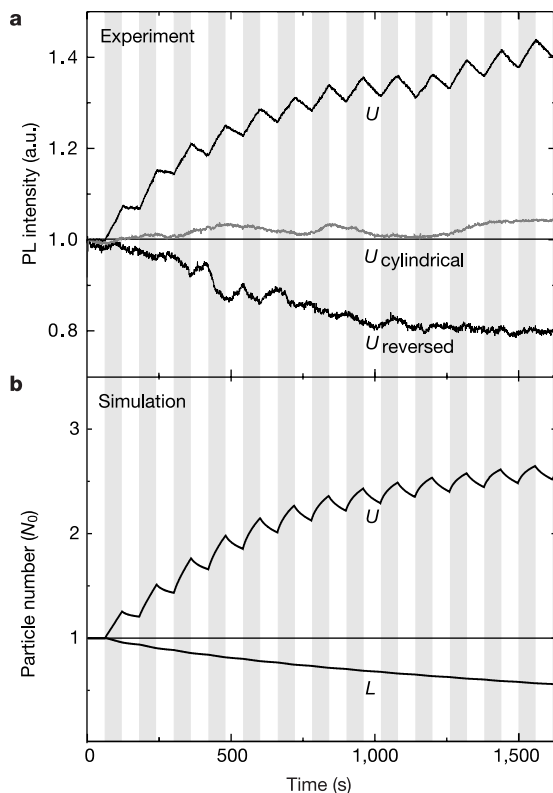


Figure 2 Photoluminescence intensity as a function of time. The pressure oscillations are toggled on and off every 60 s. The 'on' phases of the cycles are highlighted in grey. **a**, Measured intensity profile in the upper basin (U) and in a second experiment for the reversed mounted membrane of the former lower basin (U_{reversed}) as well as for cylindrical pores ($U_{\text{cylindrical}}$) for an applied root mean square (r.m.s.) pressure during the 'on' phase of 2,000 Pa, an oscillation frequency of 40 Hz and a particle diameter of $0.32 \mu\text{m}$. **b**, Simulated particle number in the two basins as a function of time. The total number of particles N in units of the initial particle number N_0 in the upper (U) and lower (L) basins were obtained by numerical integration of equation (2) using typical parameter values from ref. 17: $v_m = 0.5 \mu\text{m s}^{-1}$, $D_0 = 1.5 \mu\text{m}^2 \text{s}^{-1}$, $r = 3$, membrane thickness $150 \mu\text{m}$, basin thickness $100 \mu\text{m}$.

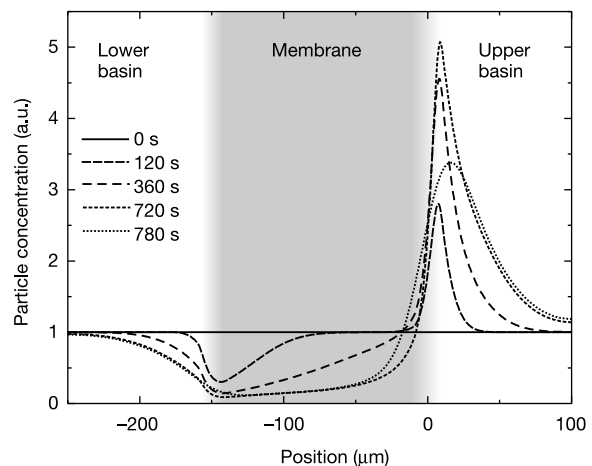


Figure 3 Simulated profile of particle concentration as a function of position for different instants in time. The particle concentration in arbitrary units was obtained by numerical integration of equation (2) using the same parameter values as in Fig. 2b. The membrane area is shaded in grey with smooth edges. As described in the text, the properties are gradually changed from the membrane to the basin to reflect the smoothing influence of the oscillations.

basin into the membrane are the reasons for the observed pseudo-saturation. The real saturation, where nearly all particles are in the upper basin, takes much longer because of the macroscopic dimensions of the lower basin and the slow particle diffusion. The occurrence of this pseudo-saturation in our measurement is a strong indication of the efficient transport inside the membrane. Only for drift values near the simulated $v = 0.5 \mu\text{m s}^{-1}$ do we expect the strong reduction in transport capacity to occur after only a few hundred seconds. In a real application device these problems could be overcome by introducing strong mixing in the basin.

The characteristic sawtooth-like profile does not in general occur for the lower basin (L) because the reduction of concentration in the lower basin itself is dominated by the diffusion process from the lower basin to the particle-depleted ratchets. The drift process removes the particles from the lower interface and, therefore, does not directly lead to a change in the number of particles in the lower basin. After a few cycles the concentration near the lower membrane surface is already reduced to a few per cent of the starting homogeneous concentration. It changes only slowly over time by the diffusion process of the particles in the lower basin and leads to the rather unstructured evolution observed in Fig. 2a (U_{reversed}).

To avoid long-term stability problems we investigated the pressure dependence with a more sophisticated pressure profile. Only a few 'on/off' cycles are performed for each amplitude, followed by a relaxation time of 200 s and then immediately followed by the next parameter set. To check reproducibility, we repeated a pressure amplitude leading to easily observable transport every fifth measurement (see Supplementary Information). The resulting dependence is depicted in Fig. 4. The error bars are estimated from the deviations in the linear fits. For low-pressure amplitudes the particles drift to the short end of the pore modulation (upper basin in Fig. 1, negative current). At 3,000 Pa the direction of the net motion switches its sign and the particles show a drift to the long end (lower basin in Fig. 1). By simply tuning the applied amplitude of the pressure oscillations the direction of transport can be reversed. For the positive direction, the experimental observation is expected to be much more difficult, as mentioned in the context of Fig. 2. Nevertheless, we can observe a few points with moderate error bars.

If the amplitude is close to zero, no transport will occur because the oscillating water-plus-particle system only moves a very short

distance compared to the length of one modulation and therefore does not feel the asymmetric pore shape. Also at high-pressure values the transport seems to diminish, as predicted by theory, although the error bars presented here do not really allow us to verify this. The experimentally observed pressure dependence strongly supports the underlying microscopic theory.

Our measurements are in qualitative agreement with the results of the theoretical calculations, suggesting that the predicted^{17,18} strong dependence of the direction of transport on particle size is likely to occur, and that the ratchet membrane might act as a massively parallel one-dimensional brownian separator¹⁸ for separation applications. Provided that problems associated with mixing and surface passivation can be resolved, the system seems well suited for the efficient and selective continuous separation of sensitive biological materials like viruses or cell fragments. As the external force is based on the flow resistance of the particles, it should be possible to separate elongated or flexible particles, provided their size is roughly in the 0.1–1 μm range. It is expected that the well developed electronic and micromechanical technology for silicon processing will allow the control of surface properties and the integration of many of the still discrete external components into 'lab on a chip' systems. In such highly integrated systems the dimensions could be drastically reduced, which would help to suppress the limiting diffusion processes in the basins and increase speed and sensitivity of the device considerably. □

Methods

Sample fabrication

The electrochemical etching of silicon is carried out in HF ($c_{\text{HF}} = 5 \text{ wt\%}$; $T = 10^\circ\text{C}$; $U = 2 \text{ V}$) under backside illumination. The substrate is n-type FZ-Si (100) with a resistivity of $5 \Omega \text{ cm}^{-1}$. Using a photolithographic pre patterning, the macropores are arranged in a triangular lattice with a pitch of $a = 6 \mu\text{m}$. After electrochemical etching, a protective SiO_2 film is grown by thermal oxidation at 800°C in an oxygen atmosphere for 2 h. This leads to a SiO_2 thickness of 20 nm. After removing the SiO_2 -layer at the backside of the silicon wafer locally by an HF-dip, the backside is removed with an anisotropic KOH-etching process. The backside of the sample is exposed to 25 wt% KOH at 90°C . Before reaching the SiO_2 etch stop, temperature is reduced to 60°C . A well-defined hydrophilic OH-terminated surface is achieved via a standard cleaning process²³: the membrane is exposed to a mixture of $\text{H}_2\text{O}:\text{NH}_3:\text{H}_2\text{O}_2 = 5:1:1$ at 80°C for 10 min.

Particles

The functionalized particles (surfactant-free, fluorescent yellow-green sulphate polystyrene latex) are provided by IDC (Interfacial Dynamics Corporation). The supplied solution is diluted after ultrasonic treatment using ultra-pure deionized water from a Millipore Milli-RX20 ($18 \text{ M}\Omega \text{ cm}^{-1}$, filter pore diameter $0.22 \mu\text{m}$).

Measurements

Particle concentration is measured using PL. For the highly diluted solutions used, the PL intensity is proportional to the number of particles in the upper basin. Excitation is done with 488-nm light from an argon laser. The PL is detected at 515 nm using a Spex 270M monochromator equipped with a Hamamatsu photomultiplier tube R928. The pressure oscillations are achieved by a membrane pump SMF 4 from ASF Thomas Industries. The applied pressure is detected with a sensor from Honeywell 26PCCFRAID. The filling level in the upper basin is measured capacitively using a Boonton 7200.

Received 21 January 2002; accepted 13 May 2003; doi:10.1038/nature01736.

- Huxley, A. F. Muscle structure and theories of contraction. *Prog. Biophys. Biophys. Chem.* **7**, 255–318 (1957).
- von Smoluchowski, M. Experimentell nachweisbare, der üblichen Thermodynamik widersprechende Molekularphänomene. *Phys. Zeitsch.* **13**, 1069–1080 (1912).
- Feynman, R. P., Leighton, R. B. & Sands, M. *The Feynman Lectures On Physics* Ch. 46 Vol. 1 (Addison-Wesley, Reading, Massachusetts, 1966).
- Faucheux, L. P., Bourdieu, L. S., Kaplan, P. D. & Libchaber, A. J. Optical thermal ratchet. *Phys. Rev. Lett.* **74**, 1504–1507 (1995).
- Marquet, C., Buguin, A., Talini, L. & Silberzan, P. Rectified motion of colloids in asymmetrically structured channels. *Phys. Rev. Lett.* **88**, 168301 (2002).
- Derényi, I. & Astumian, R. D. AC separation of particles by biased Brownian motion in a two-dimensional sieve. *Phys. Rev. E* **58**, 7781–7784 (1998).
- Rousselet, J., Salome, L., Ajdari, A. & Prost, J. Directional motion of brownian particles induced by a periodic asymmetric potential. *Nature* **370**, 446–448 (1994).
- van Oudenaarden, A. & Boxer, S. G. Brownian ratchet: molecular separations in liquid bilayers supported on patterned arrays. *Science* **285**, 1046–1048 (1999).
- Linke, H. et al. Experimental tunneling ratchets. *Science* **286**, 2314–2317 (1999).
- Switkes, M., Marcus, C. M., Campman, K. & Gossard, A. C. An adiabatic quantum electron pump. *Science* **283**, 1905–1908 (1999).

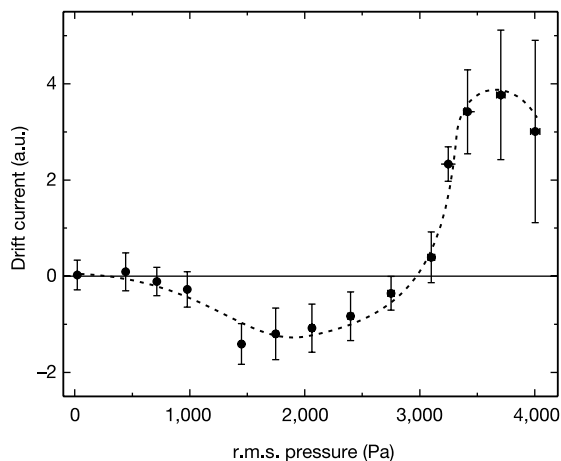


Figure 4 Drift current j_{drift} calculated from experimental results on particle transport as a function of applied pressure amplitudes. The transport of particles with a diameter of $0.1 \mu\text{m}$ diminishes for pressure values close to zero and large amplitudes. At an r.m.s. pressure of about 3,000 Pa the particle current is reversed. The direction of transport can be reversed by tuning the applied amplitude of the pressure.

11. Hänggi, P. & Bartussek, R. *Lecture Notes in Physics* Vol. 476 (eds Parisi, J., Müller, S. C. & Zimmermann, W.) 294–308 (Springer, Berlin, 1996).
12. Astumian, R. D. Thermodynamics and kinetics of a brownian motor. *Science* **276**, 917–922 (1997).
13. Astumian, R. D. & Hänggi, P. Brownian motors. *Phys. Today* **55**(11), 33–39 (2002).
14. Linke, H. (ed.) Ratchets and Brownian motors: basics, experiments and applications. *Appl. Phys. A* (Special Issue) **75**(2), (2002).
15. Cabodi, M., Chen, Y.-F., Turner, S. W. P., Craighead, H. G. & Austin, R. H. Continuous separation of biomolecules by the laterally asymmetric diffusion array with out-of-plane sample injection. *Electrophoresis* **23**, 3496–3503 (2002).
16. Müller, F. et al. Membranes for micropumps from macroporous silicon. *Phys. Stat. Sol. A* **182**, 585–590 (2000).
17. Kettner, C., Reimann, P., Hänggi, P. & Müller, F. Drift ratchet. *Phys. Rev. E* **61**, 312–323 (2000).
18. Kettner, C., Hänggi, P. & Müller, F. Verfahren und Vorrichtung zur größenabhängigen Sortierung mikroskopisch kleiner Teilchen auf der Basis von rauschinduziertem Transport. German patent pending (DE 199 07 564 A 1), submitted 22 Feb. 1999.
19. Lehmann, V. & Föll, H. Formation mechanism and properties of electrochemically etched trenches in n-type silicon. *J. Electrochem. Soc.* **137**, 653–659 (1990).
20. Lehmann, V. The physics of macropore formation in low doped n-type silicon. *J. Electrochem. Soc.* **140**, 2836–2843 (1993).
21. Schilling, J. et al. 3D photonic crystals made out of macroporous silicon by modulation of pore diameter. *Appl. Phys. Lett.* **78**, 1180–1182 (2001).
22. Lehmann, V. & Grüning, U. The limits of macropore array fabrication. *Thin Solid Films* **297**, 13–17 (1997).
23. Tong, Q. Y. & Gösele, U. *Semiconductor Wafer Bonding* 53–54 (Wiley and Sons, New York, 1999).

Supplementary Information accompanies the paper on www.nature.com/nature.

Acknowledgement We thank U. Gösele for backing the ratchet project over many years. We also gratefully acknowledge discussions on the theory of the ratchet-effect with P. Hänggi, Ch. Kettner, P. Reimann and R. Eichhorn as well as critical reading of the manuscript by K. Scheerschmidt and R. B. Wehrspohn.

Competing interests statement The authors declare that they have no competing financial interests.

Correspondence and requests for materials should be addressed to F.M. (Frank.Mueller@mpi-halle.de).

High ³He/⁴He ratios in picritic basalts from Baffin Island and the role of a mixed reservoir in mantle plumes

Finlay M. Stuart*, Solveigh Lass-Evans*†, J. Godfrey Fitton† & Robert M. Ellam*

* Isotope Geosciences Unit, Scottish Universities Environmental Research Centre, East Kilbride G75 0QF, UK

† School of GeoSciences, University of Edinburgh, Edinburgh EH9 3JW, UK

The high ³He/⁴He ratio of volcanic rocks thought to be derived from mantle plumes is taken as evidence for the existence of a mantle reservoir that has remained largely undegassed since the Earth's accretion^{1–3}. The helium isotope composition of this reservoir places constraints on the origin of volatiles within the Earth and on the evolution and structure of the Earth's mantle. Here we show that olivine phenocrysts in picritic basalts presumably derived from the proto-Iceland plume at Baffin Island, Canada, have the highest magmatic ³He/⁴He ratios yet recorded. A strong correlation between ³He/⁴He and ⁸⁷Sr/⁸⁶Sr, ¹⁴³Nd/¹⁴⁴Nd and trace element ratios demonstrate that the ³He-rich end-member is present in basalts that are derived from large-volume melts of depleted upper-mantle rocks. This reservoir is consistent with the recharging of depleted upper-mantle rocks by small volumes of primordial volatile-rich lower-mantle material at a thermal boundary layer between convectively isolated reservoirs. The highest ³He/⁴He basalts from Hawaii and Iceland plot on the observed mixing trend. This indicates that a ³He-recharged depleted mantle (HRDM) reservoir may be the principal source

of high ³He/⁴He in mantle plumes, and may explain why the helium concentration of the 'plume' component in ocean island basalts is lower than that predicted for a two-layer, steady-state model of mantle structure.

Ocean island basalts (OIB) derived from mantle plumes commonly have ³He/⁴He ratios that are higher than mid-ocean ridge basalts (MORB) that originate in the upper, asthenospheric mantle^{1–3}. High ³He/⁴He and solar-like Ne isotope ratios⁴ reflect a higher proportion of primordial volatiles in the source region and, in the current paradigm, indicate that plumes tap a deep mantle reservoir that is significantly less degassed than the asthenospheric mantle. Although a number of locations have been proposed for this reservoir⁵, a lower mantle that has been convectively isolated below the 670-km seismic discontinuity for the lifetime of the Earth⁶ is consistent with the mass balance of the depleted mantle and continental crust⁷. However, layered mantle models are seemingly at odds with seismic studies that demonstrate convective flow across the 670-km boundary⁸ and require a 100- to 200-fold depletion of the He concentration in the upper, degassed mantle relative to the deep undegassed mantle reservoir⁶. Plume-derived OIB from, for example, Loihi seamount, Hawaii, have lower He concentrations than basalts from the degassed upper mantle² and have posed a persistent problem for a unified geochemical model of Earth structure⁶. The apparent paradox can be explained, at least in part, by more extensive degassing of ocean island basalts⁹. However, basalts from Iceland and the Hawaiian islands have linear, rather than strongly hyperbolic, He–Pb isotope mixing arrays that are consistent with relatively small He concentration contrasts between the degassed mantle and less degassed (high ³He/⁴He) mantle reservoirs^{9,10}.

Picritic basalts erupted on Baffin Island, northeast Canada, 61 Myr ago correlate with the Anaanaa Member of the Vaigat Formation in West Greenland¹¹, and are among the earliest manifestations of the ancestral Iceland mantle plume¹². Trace-element and Sr–Nd isotope ratios show that they were generated by mixing of two discrete sources; relatively depleted mantle with (La/Sm)_n < 1, ⁸⁷Sr/⁸⁶Sr ≈ 0.7030, ¹⁴³Nd/¹⁴⁴Nd ≈ 0.5130, and relatively enriched mantle with (La/Sm)_n > 1, ⁸⁷Sr/⁸⁶Sr ≈ 0.7042 and ¹⁴³Nd/¹⁴⁴Nd ≈ 0.51282 (ref. 13). The depleted basalts are similar to the most depleted Icelandic basalts and North Atlantic MORB¹⁴. The enriched basalts are similar to, though slightly more extreme (higher ⁸⁷Sr/⁸⁶Sr and lower ¹⁴³Nd/¹⁴⁴Nd ratios) than the most enriched basalts erupted by the Iceland plume and across the North Atlantic igneous province¹⁵.

The isotopic composition of He released by *in vacuo* crushing olivine phenocrysts from picritic basalts from three stratigraphically distinct cliff sections in northeast Baffin Island (Table 1) ranges from 14.4R_a to 49.5R_a (where R_a is the atmospheric ³He/⁴He ratio; 1.39 × 10⁻⁶). These ratios are far higher than MORB values and extend the range measured in contemporaneous picrites from West Greenland¹⁶. The high ratios cannot result from contamination by *in situ* cosmogenic ³He because (1) *in vacuo* crushing does not release cosmogenic He from the olivine lattice¹⁷, (2) cosmogenic ³He production was negligible because the samples were collected from eroding, near-vertical sea cliff faces, and (3) the ³He/⁴He of powders produced by crushing are systematically lower than crush values (Table 1) indicating that radiogenic He dominates the olivine lattice. Nucleogenic ³He production from ⁶Li is negligible in Palaeocene basalts¹⁶.

Crush release of radiogenic ⁴He in the olivine lattice and melt inclusions by post-eruptive U and Th decay tends to lower ³He/⁴He, so measured ratios may underestimate the source ³He/⁴He. Any such effect would be most pronounced in samples with the lowest He content. ³He/⁴He are not correlated with He concentration (Table 1), implying that post-eruptive radiogenic He is insignificant to the crush-release He. Crustal contamination of the basalts by amphibolite- and granulites-facies basement rocks would also lower